Joint Scale-Lag Diversity in Wideband Mobile Direct Sequence Spread Spectrum Systems

Adam R. Margetts, *Member, IEEE,* Philip Schniter, *Senior Member, IEEE,* and Ananthram Swami, *Senior Member, IEEE*

***Abstract*— We consider the effect of mobility on a wideband direct sequence spread spectrum (DSSS) communication system, and study a scale-lag Rake receiver capable of leveraging the diversity that results from mobility. A wideband signal has a large bandwidth-to-center frequency ratio, such that the typical narrowband Doppler spread assumptions do not apply to mobile channels. Instead, we assume a more general temporal scaling phenomenon, i.e., a dilation of the transmitted signal's time support. Based on a uniform ring of scatterers model, we determine that the wideband scattering function, which quantifies the average scale spreading, has a "bathtub-shaped" scale profile. We compare the performances of a scale-lag Rake and a frequency-lag Rake, each capable of leveraging the diversity that results from mobility. Such analysis applies, for example, to ultra-wideband (UWB) radio frequency channels and underwater wideband acoustic channels.**

***Index Terms*— Mobile wireless communication, scale-lag diversity, spread spectrum, wideband systems.**

I. Introduction

WIDEBAND communication systems are defined as having a fractional bandwidth—the ratio of single-sided bandwidth to center frequency—that exceeds 0.20 [1] [2]. Otherwise, the system is called *narrowband*. We are interested in studying the effect of mobility (i.e., temporal variation in the physical geometries between transmitter, receiver, and scatterers) on wideband communications systems and in designing transceivers capable of leveraging the potential diversity gains that result from multipath propagation in mobile environments.

First, it is important to note that the combined effects of multipath and mobility on transmitted signals are modeled quite differently for wideband systems than for their narrowband counterparts. For example, in narrowband systems with a dense ring of scatterers surrounding the receiver, mobility imparts a spreading of the signal in the frequency-domain that is commonly referred to as Doppler spreading [3, p. 809]. In wideband communication systems employing direct sequence spread spectrum (DSSS)—the focus of this manuscript—the effects of mobility in the multipath mobile environment are not well described by frequency-domain spreading, but rather by time-domain *scale spreading*. Note that scale-spreading arises from the same fundamental mechanism that causes Doppler spreading. For example, changing the time scale of a single sinusoid is equivalent to shifting the signal in frequency. By scale spreading, we mean that several copies of the transmitted signal combine at the receiver, each with a different dilation of the time support of the original signal. In addition, each copy may be attenuated and temporally delayed by a different amount.

When the different propagation paths are characterized by independent dilations and delays, the fading inherent to multipath propagation can be mitigated by using diversity reception. For wideband DSSS signaling, we propose a *scale-lag Rake receiver* that extracts this diversity.[1] The scale-lag Rake employs a basis composed of shift-dilates of the transmitted waveform in order to match the scale-lag spreading induced by the wideband channel. In general, the transmit waveform could be designed to optimally enable the scale-lag diversity; however, for practical considerations, we constrain the transmit waveform to be a DSSS signal. The analysis can be applied to underwater acoustic systems [4] as well as to radio frequency ultra-wideband (UWB) systems [5]. In particular, this paper considers mobile wideband systems with limited available lag diversity where extracting dilation diversity has the potential to significantly improve performance [6].

The rest of the paper is organized as follows. Section II describes the DSSS waveform and defines the transformation used to model the input-output characteristics of the wideband channel. Section III motivates the scale-lag Rake receiver and discusses the scale-resolution property of a wideband DSSS waveform. Furthermore, a low complexity implementation of the scale-lag basis projection is proposed. In Section IV, the wideband scattering function, which quantifies the scale-lag channel energy profile, is examined and scale-lag diversity is defined. Section V supports the analysis by providing numerical results for a system employing second-derivative Gaussian chip pulses. Finally, we provide conclusions in Section VI.

II. System Model

A. Transmit Signal

Throughout, we assume baseband DSSS signaling, where the transmitted signal $s(t)$ results from linearly modulating a

[1]The possibility of a scale-lag receiver was mentioned in [3], but no details were developed.

Manuscript received March 4, 2005; revised October 25, 2005, June 27, 2006, and March 21, 2007; accepted August 15, 2007. The associate editor coordinating the review of this paper and approving it for publication was S. Zhou. This work was supported by the Ohio Space Grant Consortium and by the Office of Naval Research. Portions of this work were presented at the 2004 Asilomar Conference on Signals, Systems, and Computers, and at the 2005 International Conference on Acoustics, Speech, and Signal Processing.

A. Margetts is with MIT Lincoln Laboratory, 244 Wood St., Lexington, MA 02420 USA (e-mail: margetts@ieee.org).

P. Schniter is with the Department of Electrical and Computer Engineering, The Ohio State University, 2015 Neil Ave., 616 Dreese Laboratories, Columbus, OH 43210 USA (e-mail: schniter@ece.osu.edu).

A. Swami is with the Army Research Laboratory, 2800 Powder Mill Rd., Adelphi, MD 20783 USA (e-mail: a.swami@ieee.org).

Digital Object Identifier 10.1109/TWC.2007.05141.

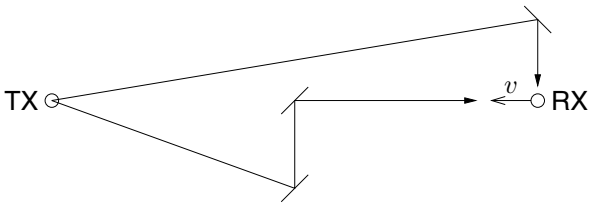

Fig. 1. Wireless channel diagram with two equal-length propagation paths from the transmitter to the receiver. The receiver is traveling with velocity v.

sequence of BPSK symbols $\{b_k\}$ with a wideband signature waveform $x(t)$:

$$s(t) \quad = \quad \sum_{k=0}^{N_b-1} b_k x(t - kT_b), \tag{1}$$

In (1), N_b is the number of transmitted bits, T_b is the bit spacing, and $b_k \in \{-\sqrt{E_b}, \sqrt{E_b}\}$, where E_b is the energy per bit.

The wideband DSSS signature waveform takes the form

$$x(t) \quad = \quad \frac{1}{\sqrt{N_p}} \sum_{i=0}^{N_p-1} c_i p(t - iT_o), \tag{2}$$

where $p(t)$ is the unit-energy *chip pulse*, $\{c_i\}_{i=0}^{N_p-1}$ is the length-N_p pseudo-noise (PN) *chip sequence*, and $T_o = \frac{T_b}{N_p}$ is the *chip spacing*. The spreading sequences in this paper are modeled as random to facilitate the analysis. Since we consider baseband signaling, all signals and parameters are real valued. We assume that the chip pulse $p(t)$ is bandpass with spectral peak f_o Hz, single-sided bandwidth $W \approx 2f_o$ Hz, and duration $T_p \approx f_o^{-1}$ seconds, where typically $T_p < T_o$. To model time-hopping [5] or episodic signaling [7], the PN sequence $\{c_i\}$ may be chosen from a ternary alphabet $c_i \in \{-\frac{1}{\sqrt{q}}, 0, \frac{1}{\sqrt{q}}\}$, where the non-zero chip probability q is chosen so that $\mathrm{E}[c_i^2] = 1$. See [8], [9] for more details on the construction of ternary sequences.

B. Wideband Channel Representation

The wideband channel output $r(t)$, due to input $s(t)$, can be modeled as [10]

$$r(t) \quad = \quad \underbrace{\iint \mathcal{L}(a,\tau) \frac{1}{\sqrt{a}} \, s\left(\frac{t-\tau}{a}\right) da \, d\tau}_{\mathcal{L}\{s(t)\}} + w(t), \tag{3}$$

where $\mathcal{L}(a,\tau)$ is the *wideband channel kernel* and $w(t)$ is zero-mean additive white Gaussian noise (AWGN) with two-sided power spectral density σ_w^2. The model (3) allows for a continuum of paths, where each path is associated with a *propagation delay* of τ seconds and a *dilation factor* of a. In particular, the kernel $\mathcal{L}(a,\tau)$ quantifies the contribution of all paths with dilation/delay (a,τ). Note that, since the wideband transformation $\mathcal{L}\{\cdot\}$ is *not* time-invariant, its eigenfunctions are *not* sinusoids. Note also that $\mathcal{L}\{\cdot\}$ subsumes wideband time-selective fading, wideband frequency-selective fading, and wideband doubly selective fading.

We illustrate the function of the wideband channel kernel $\mathcal{L}(a,\tau)$ with the simple two-path noiseless example shown in Fig. 1. Suppose that the two paths have equal length: $d = c\tau'$, where c is the speed of wave propagation and τ' is the temporal lag from transmitter to receiver. With the receiver moving at velocity v, the path arriving perpendicular to the direction of motion experiences no dilation ($a = 1$), while the path arriving parallel to the direction of motion experiences a dilation of $a' < 1$. Hence, the received signal can be written as $r(t) = s(t-\tau') + \frac{1}{\sqrt{a'}} s(\frac{t-\tau'}{a'})$, obeying (3) under the wideband channel kernel $\mathcal{L}(a,\tau) = \delta(a-1)\delta(\tau-\tau') + \delta(a-a')\delta(\tau-\tau')$ with $\delta(\cdot)$ denoting the Dirac delta function. In this model, a path arriving at an angle of ξ radians (relative to the direction of receiver motion) will experience a dilation factor of $a' = 1 - \frac{v}{c}\cos(\xi)$.

Finite velocities and path losses imply that the wideband channel kernel $\mathcal{L}(a,\tau)$ has non-zero support on the compact set $\Omega = \{(a,\tau) : a_{\min} \le a \le a_{\max}, \ 0 \le \tau \le \tau_{\max}\}$, where $a_{\min}$ and $a_{\max}$ are the *minimum* and *maximum dilation*, respectively, and where $\tau_{\max}$ is the *maximum delay spread*. By convention, we assume that the shortest path has time delay of zero. Some channels may be considered *sparse*, such that $\mathcal{L}(a,\tau)$ is non-zero on a small fraction of the set Ω [11]. We define the *effective delay spread* $\tau_{\sup}$ to be the measure of the non-zero lag support. The minimum dilation and maximum dilation can be written $a_{\min} = 1 - v_{\max}/c$ and $a_{\max} = 1 + v_{\max}/c$, respectively, where $v_{\max}$ is the maximum relative velocity.

An important system parameter is the (single-sided) *scale spread*: $\gamma_{\max} := \frac{a_{\max} - a_{\min}}{2} = v_{\max}/c = a_{\max} - 1$, which defines the maximum deviation from unit temporal dilation. As we shall see, the *normalized scale spread* $\gamma_{\max} T_b f_o = \frac{v_{\max}}{c} T_b f_o$ quantifies the effect of mobility on a wideband communication system. This parameter is analogous to the *normalized Doppler spread* $f_{\max} T_b = \frac{v_{\max}}{c} T_b f_c$, which quantifies the effect of mobility on a narrowband communication system. There, f_c denotes the carrier frequency and $f_{\max} = \frac{v_{\max}}{c} f_c$ denotes the single-sided Doppler frequency spread [12, p. 809].

Typical values of scale spread $\gamma_{\max}$ can be quite large in underwater acoustic channels. In particular, the numerical experiments in Section V demonstrate that the wideband mobility allows significant diversity gain when $\gamma_{\max} T_b f_o \ge 0.01$. For example, $\gamma_{\max} = 0.002$ results from[2] $v_{\max} = 11$ km/hr, from which $\gamma_{\max} T_b f_o = 0.01$ can be obtained for, e.g., an underwater DSSS system with data rate $T_b^{-1} = 10$ bps and bandwidth 100 Hz. The latter rate should be adequate for environmental monitoring applications which track slowly varying parameters such as temperature or salinity. Though typical values of scale spread $\gamma_{\max}$ may be extremely small for mobile RF channels, the effect of this scale spread can be

[2]As described in [13], mobility in underwater applications could arise from wind-induced wave motion of a receiver mounted on a floating buoy. Using the rule $h_{\text{rms}} f_{\text{wave}} = 0.01 v_{\text{wind}}^{1.5}$ [13], where h_{rms} denotes RMS wave height in meters, f_{wave} denotes wave frequency in Hz, and v_{wind} denotes wind velocity in m/s—and assuming that the buoy bobs vertically, with the transmitter located θ radians from the axis of motion—it is straightforward to show that a maximal rate of path length variation $v_{\max}$ m/s corresponds to a wind speed of $v_{\text{wind}} = (\frac{100 v_{\max}}{2.8\pi \cos(\theta)})^{2/3}$ m/s. Using this relationship with $\theta = \pi/6$, a mobility of $v_{\max} = 11$ km/hr corresponds to a wind speed of 42 km/hr.

significant when $T_b f_o$, the signal's time-bandwidth product, is large enough. As an example, $v_{\max} = 67.5$ km/hr yields $\gamma_{\max} = 6.25 \times 10^{-8}$ in RF channels, from which $\gamma_{\max} T_b f_o = 0.01$ can be obtained for, e.g., a DSSS system with data rate $T_b^{-1} = 25$ kbps and bandwidth $W = 8$ GHz.

We shall see that the *normalized effective delay spread* $\tau_{\sup} f_o$ quantifies the effect of multipath time-dispersion in wideband systems. Since $f_o \approx W/2$, the normalized effective delay spread can be approximated by $\frac{1}{2}\tau_{\sup} W$, which is known to quantify the effect of time-dispersion in narrowband systems. As an example of a system with limited lag diversity, if we choose $\tau_{\max} = \tau_{\sup} = 10$ ms in the previously described acoustic example[3], we find a normalized effective delay spread of $\tau_{\sup} f_o = 0.5$.

From the previous RF example, given a maximum delay spread of $\tau_{\max} = 2.5$ μs, we find a normalized maximum delay spread of $\tau_{\max} f_o = 1.0 \times 10^4$. However, vehicular channels are often sparse, as shown in [11]. For example, in 95% of measured channels only 5 rays were significant[4], while in 79% of measured channels only 2 rays were significant. Since, at bandwidth W Hz, each ray contributes $\frac{1}{2W}$ seconds to the effective delay spread $\tau_{\sup}$, a 2-ray channel would yield a normalized effective delay spread of $\tau_{\sup} f_o = 0.5$. These diverse rays can be resolved by a DSSS system as shown in Section III.

Throughout the paper, we assume that the maximum delay spread is much less than the symbol spacing, i.e., $\tau_{\max} \ll T_b$, in which case guardbands can be inserted to prevent inter-symbol interference (ISI) with a small loss in spectral efficiency. This assumption is reasonable for DSSS with large processing gain and is often made for impulse-radio UWB RF systems [14, p.34] and DSSS underwater acoustic systems [4]. It can be confirmed that $\tau_{\max} = 0.1 T_b$ for the previously described underwater acoustic example and $\tau_{\max} = 0.0625 T_b$ for the previously described RF example.

III. Scale-Lag Rake Receiver

A. Wideband Scale-Lag Canonical Model Representation

Sayeed and Aazhang [15] derived a narrowband canonical model for parsimonious representation of a narrowband baseband-equivalent received signal and, after making statistical assumptions on the narrowband baseband-equivalent channel kernel, analyzed the performance of a *frequency-lag Rake* receiver, which exploits Doppler-lag channel diversity in a mobile spread-spectrum system. Motivated by the narrowband canonical model, Balan et al. [3] derived a canonical model for the wideband transformation. A similar wideband decomposition was proposed independently in [16].

The wideband canonical model parameterizes the wideband transformation as a weighted sum of delay and dilation operations [3]:

$$\mathcal{L}\{s(t)\} = \sum_m \sum_n l_{m,n} \frac{1}{a_\star^{m/2}} s\left(\frac{t - n t_\star a_\star^m}{a_\star^m}\right), \qquad (4)$$

[3]A delay spread of 10 ms is said to be typical for underwater acoustic channels [13].

[4]We reason that the number of rays in our example RF channel is similar to the number of rays in the measured 19 MHz-bandwidth channels in [11], since [11] concludes "a majority of the delay spread seen in the current environment is due to single reflections from large man-made scatterers."

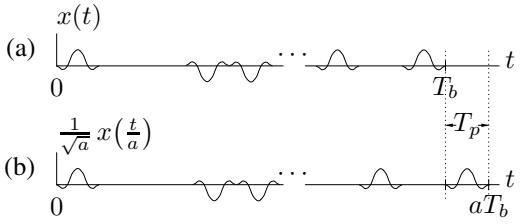

Fig. 2. Illustration of waveform $x(t)$ (a) before and (b) after dilation by factor a.

where the canonical weighting coefficients $l_{m,n}$ are given by,

$$l_{m,n} = \int_0^{\tau_{\max}} \int_{a_{\min}}^{a_{\max}} \mathcal{L}(a,\tau) \operatorname{sinc}\left(n - \frac{\tau}{a t_\star}\right) \operatorname{sinc}\left(\frac{\ln(a)}{\ln(a_\star)} - m\right) da\, d\tau. \qquad (5)$$

The quantities $a_\star$ and $t_\star$ are the channel's *dilation spacing* and *translation spacing* parameters, respectively. See [3] for more details. Note that (5) follows from (3)-(4).

The wideband canonical representation (4) implies that, in the presence of AWGN at the receiver, a bank of correlators matched to shift-dilates of the wideband signature waveform (i.e., the scale-lag Rake) will produce a set of (possibly correlated) sufficient statistics for optimal reception [12, Ch 5]. Although [3] suggested the possibility of a scale-lag Rake receiver for the wideband case, it was never developed. Our main contribution is to develop and study the scale-lag Rake receiver for the wideband channel.

B. Scale-Lag Resolution

The scale-lag resolution properties of a wideband DSSS signal $x(t)$ can be determined by studying the *wideband ambiguity function* $\chi(a,\tau)$ [17], defined as

$$\chi(a,\tau) := \left\langle x(t), \frac{1}{\sqrt{a}} x\left(\frac{t-\tau}{a}\right) \right\rangle \qquad (6)$$

where $\langle f(t), g(t) \rangle := \int_{-\infty}^{\infty} f(t) g(t) dt$ is the inner product.

We define the *minimum resolvable lag* τ_o to be the smallest $\tau > 0$ such that $\chi(1,\tau) = 0$, and the *minimum resolvable dilation* α_o to be the smallest $a > 1$ such that $\chi(a,0) = 0$; the *minimum scale resolution* is defined as $\beta_o := \alpha_o - 1$. Below, we show that these resolution quantities are related to the chip-pulse duration T_p—or, equivalently, the peak frequency f_o—and to the symbol spacing T_b. The minimum resolvable lag and the minimum scale resolution will be used as guidelines in the sequel to construct the basis functions for the scale-lag Rake receiver.

An often used rule-of-thumb is that a linear Rake receiver can resolve multipath with inter-arrival lag differences on the order of T_p seconds [12, p. 841]. This is verified by the following proposition.

Proposition 1: The mean and variance of the ambiguity function $\chi(1,\tau)$ of the wideband DSSS signal $x(t)$ in (2) vanish for $\tau \geq T_p$.

Proof: See Appendix I. ■

It immediately follows from Proposition 1 that the minimum resolvable lag τ_o has an upper bound given by $\tau_o \leq T_p$. Next,

the scale resolution property of a DSSS signal is linked to the time-bandwidth product. Let a result in a dilation greater than or equal to one chip-pulse duration T_p (illustrated by Fig. 2), i.e.,

$$aT_b - T_b \quad \geq \quad T_p \;\Leftrightarrow\; a \geq 1 + \frac{T_p}{T_b}. \tag{7}$$

Now consider the following proposition, which gives a rule-of-thumb for the minimum resolvable dilation α_o.

Proposition 2: The mean and variance of $\chi(a,0)$ vanish for $a \geq 1 + \frac{T_p}{T_b}$ if and only if the chip pulse $p(t)$ has zero DC component.

Proof: See Appendix I. ■

From Proposition 2, we see that, for zero-DC pulses, the minimum scale resolution is upper bounded by $\beta_o \leq \frac{T_p}{T_b}$. Since the chip-pulse duration T_p and the peak frequency f_o are inversely proportional, we can say that the scale resolution β_o is on the order of $(T_b f_o)^{-1}$—the inverse of the time-bandwidth product.

C. Example: Second-Derivative Gaussian Chip Pulse

We now use a second-derivative Gaussian chip pulse to illustrate the scale and lag resolution properties of a DSSS signal. The pulse waveform is defined as [18]

$$p(t) \quad = \quad \frac{\sqrt{f_o}\sqrt[4]{32\pi}}{\sqrt{3}}\left[1 - 2(\pi f_o t)^2\right] e^{-(\pi f_o t)^2}, \tag{8}$$

with Fourier transform

$$P(f) \quad = \quad \frac{\sqrt{f_o}\sqrt[4]{32\pi}}{\sqrt{3}} \frac{2}{\sqrt{\pi f_o^2}} \left(\frac{f}{f_o}\right)^2 e^{-\frac{f^2}{f_o^2}}. \tag{9}$$

Time and frequency plots of the second-derivative Gaussian are shown in Fig. 3. From Fig. 3(a), we argue that the chip pulse duration[5] is roughly $T_p = \frac{2}{f_o}$ seconds. From Fig. 3(b), we see that the chip pulse (8) has zero DC component[6] and confirm that the peak frequency equals f_o.

It is shown in Appendix I that, for large spreading gain N_p and practical values of dilation (i.e., $a \approx 1$),[7] the wideband ambiguity function can be approximated in the mean-square sense as

$$\begin{aligned} \chi(a,\tau) \quad &\approx \quad \bar{\chi}(a,\tau), \\ &:= \quad \int_0^1 \chi_p(1, \tau + (a-1)zT_b)dz \end{aligned} \tag{10}$$

where

$$\chi_p(a,\tau) \quad := \quad \left\langle p(t), \frac{1}{\sqrt{a}} p\left(\frac{t-\tau}{a}\right)\right\rangle \tag{11}$$

is the wideband ambiguity function of the chip pulse $p(t)$. The ambiguity function for the second derivative Gaussian pulse

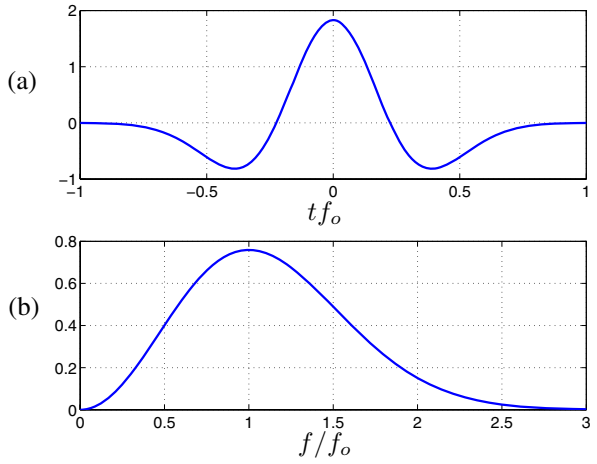

Fig. 3. Plot of (a) $p(t)$ (time domain) and (b) $P(f)$ (frequency domain) for the second-derivative Gaussian chip pulse (i.e., "Mexican hat wavelet") defined in (8).

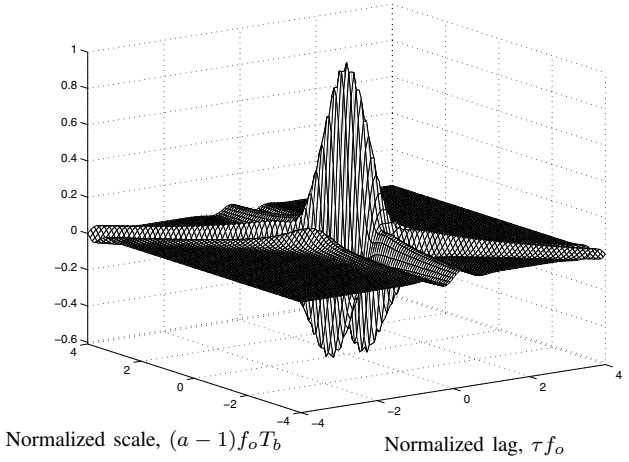

Fig. 4. Approximate wideband ambiguity function $\bar{\chi}(a,\tau)$ with the second-derivative Gaussian chip pulse (8).

(8) can be written as [21, p. 63]

$$\begin{aligned} &\chi_p(a,\tau) = \\ &\quad f(a)\left(4\pi^4 f_o^4 \tau^4 - 12\pi^2 f_o^2 \tau^2 (1+a^2) + 3(1+a^2)^2\right) \\ &\quad \exp\left(-\frac{\pi^2 f_o^2 \tau^2}{1+a^2}\right), \end{aligned} \tag{12}$$

where $f(a) := \frac{4}{3}\sqrt{\frac{2a^5}{(1+a^2)^9}}$. Plugging (12) into (10) yields an approximation for the wideband ambiguity function (6), which is plotted in Fig. 4. (Note that the approximation $\bar{\chi}(a,\tau)$ is not directly a function of the chip spacing T_o.) For comparison, Fig. 5 plots the deterministic wideband ambiguity function $\chi(a,\tau)$ corresponding to a length-128 i.i.d. random binary chip sequence $\{c_i\}$ with chip spacing $T_o = T_p$ (i.e., non-overlapping chips). Note the similarity between Fig. 4 and Fig. 5.

We now find the minimum resolvable dilation α_o and minimum resolvable lag τ_o for DSSS signaling over second-derivative Gaussian chip pulses. To do so, we examine the

[5]Some authors [19], [20] define duration differently and conclude $T_p = \frac{7}{\pi f_o \sqrt{2}} = \frac{1.58}{f_o}$.

[6]There exist other zero-DC pulses, e.g. the modified duobinary pulse [12, p. 563].

[7]Recall that $1 - \frac{v_{\max}}{c} \leq a \leq 1 + \frac{v_{\max}}{c}$, where, usually, $\frac{v_{\max}}{c}$ is very small compared to 1.

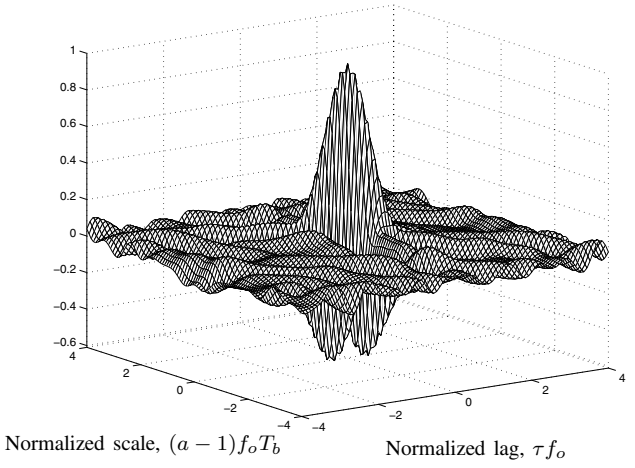

Fig. 5. Deterministic wideband ambiguity function $\chi(a,\tau)$ of a DSSS waveform $x(t)$ composed of a length-128 i.i.d. random binary sequence modulating second-derivative Gaussian chip pulses with chip spacing $T_o = \frac{2}{f_o}$.

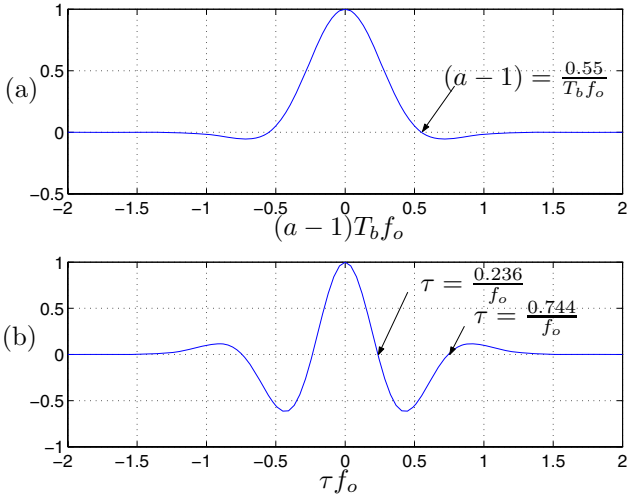

Fig. 6. Plot of (a) $\bar{\chi}(a,0)$ and (b) $\bar{\chi}(1,\tau)$ for DSSS waveform employing second-derivative Gaussian chip-pulses.

cross-sections $\bar{\chi}(a,0)$ and $\bar{\chi}(1,\tau)$, plotted in Fig. 6(a) and Fig. 6(b), respectively. From Fig. 6(a), we see that the minimum resolvable dilation is approximately $\alpha_o = 1 + \frac{0.55}{T_b f_o}$, yielding minimum scale resolution $\beta_o = \frac{0.55}{T_b f_o}$. We also see that $\bar{\chi}(a,0)$ approaches zero again at $a = 1 + \frac{1}{T_b f_o}$ and vanishes for $a \geq 1 + \frac{2}{T_b f_o} = 1 + \frac{T_p}{T_b}$, as predicted by Proposition 2. From Fig. 6(b), we see that the minimum resolvable lag is approximately $\tau_o = \frac{0.236}{f_o}$. We also see that $\bar{\chi}(1,\tau)$ approaches zero again at $\tau = \frac{0.744}{f_o}$ and vanishes for $\tau \geq \frac{2}{f_o} = T_p$, as predicted by Proposition 1.

D. Connection to Radar, Sonar, and Wavelets

The reader will notice that if $x(t)$ satisfies the wavelet admissibility conditions [22, p. 125], then $\chi(a,\tau)$ is the continuous wavelet transform (CWT) with respect to $x(t)$. It is easily verified that if the chip pulse $p(t)$ is admissible, then the waveform $x(t)$ is also admissible. A necessary condition of admissibility is for the waveform to have a zero at DC; hence, an arbitrarily chosen wavelet will satisfy Proposition 2. In this paper, wavelet sequences are used to extract scale diversity from the channel; wavelets have also been used for time-varying system identification [23], [24]. The connection between wavelet analysis and wideband processing for Radar and Sonar is studied in [25], and experimental results are reported in [26].

The affect of time dilation on spread-spectrum signals is sometimes called "code Doppler." A study of the effect of code Doppler on timing acquisition was performed in [27]. We are not aware of any attempts to exploit the presence of code Doppler for diversity gain. Code Doppler will also occur if there is a sampling frequency mismatch between the transmitter digital to analog converter (DAC) and the receiver analog to digital converter (ADC), in which case every path is dilated by the same amount.

The scale and lag resolution analysis we have performed for DSSS signals could be applied to Radar/Sonar estimation of target velocity and range. Consider the following recent papers on the topic. An exploration on the connection of the wideband ambiguity function (6) for arbitrary motion (not just constant velocity) and its constant-velocity narrowband approximation is found in [28]. In [29], the authors investigate the dilation resolution properties of random wideband signals, which are generated via a Gaussian noise source. In [30], a ternary-modulated sequence was used to estimate range and velocity. In [31], the authors estimate range by determining when the pulse first arrives. In [32], a Cramer-Rao lower bound (CRLB) on the estimation error of velocity and range via wideband ambiguity function analysis is calculated based on the Mellin transform [33]. One avenue of future work is to design optimal CRLB-minimizing chip-pulses and sequences by applying the Mellin transform analysis in [32] to our ambiguity-function approximations.

E. Choice of Rake Basis Functions

Motivated by the scale-lag wideband channel parameterization in Section III-A and the scale-lag resolution properties in Section III-B, we choose, as basis functions for demodulating the k^{th} bit, the set of dilated-delayed versions of the DSSS waveform $x(t)$ [c.f., (2)]:

$$x_{m,n}^{(k)}(t) = \frac{1}{\sqrt{a_o^m}} x\left(\frac{t - nt_o a_o^m - kT_b}{a_o^m}\right), \qquad (13)$$

where a_o is the *dilation-spacing* parameter and t_o is the *translation-spacing* parameter (c.f. Section III-A). We define $\gamma_o := a_o - 1$ as the *scale-spacing* parameter.

Recalling the relationship between the minimum resolution quantities (α_o, τ_o) and the system parameters (f_o, T_b), we set the scale-spacing and translation-spacing equal to $\gamma_o = \frac{k_\gamma}{T_b f_o}$ and $t_o = \frac{k_t}{f_o}$, respectively, where k_γ and k_t are Rake design parameters. Note that, for the case of second-derivative Gaussian chip pulses, the choices $k_\gamma = 0.55$ and $k_t = 0.236$ yield dilation-spacing and translation-spacing equal to the minimum resolvable dilation and lag, respectively.

The *scale-lag Rake receiver* projects the received signal onto the scale-lag basis functions $\{x_{m,n}^{(k)}(t)$ for $(m,n) \in \mathcal{I}\}$

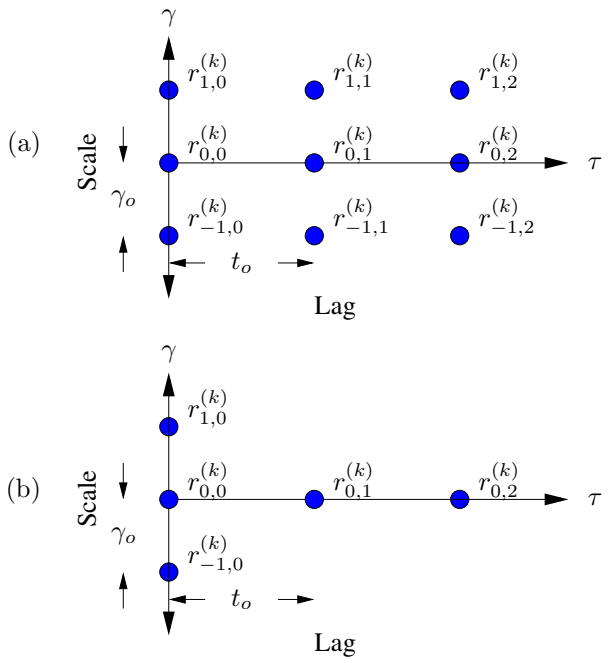

Fig. 7. Example scale-lag Rake configurations: (a) rectangular, and (b) "T-shaped".

and subsequently combines the projection coefficients to infer the k^{th} bit. The index set $\mathcal{I}$ specifies the coordinates of active Rake fingers. For example, Fig. 7(a) shows a Rake with a rectangular grid of scale-lag fingers and Fig. 7(b) shows a Rake with two active non-trivial scale fingers. Note that the conventional lag-only Rake is a special case of the scale-lag Rake with $\mathcal{I} = \{(0,n) : n = 0, \ldots, N\}$, i.e., with only trivial scale fingers. Note also that, for typical values of dilation-spacing (i.e., $a_o \approx 1$), a Taylor series approximation around the point $a_o = 1$ gives $a_o^m \approx 1 + m(a_o - 1) = 1 + m\gamma_o$. Thus $\{x_{m,n}^{(k)}(t)\}_{m\in\mathbb{Z}}$ constitutes an approximately uniform sampling of the scale domain with sampling interval γ_o.

Using the wideband channel transformation (3), we now analyze $\{r_{m,n}^{(k)}\}$, the scale-lag Rake projection coefficients for the k^{th} bit:

$$\begin{aligned} r_{m,n}^{(k)} &= \langle x_{m,n}^{(k)}(t), r(t)\rangle, \\ &= \sum_{l=0}^{N_b-1} b_l \underbrace{\left\langle x_{m,n}^{(k)}(t), \mathcal{L}\{x(t-lT_b)\}\right\rangle}_{\approx 0, \text{ for } l\neq k \text{ since } \tau_{\max}\ll T_b} + \underbrace{\langle x_{m,n}^{(k)}(t), w(t)\rangle}_{w_{m,n}^{(k)}}, \\ &\approx b_k \underbrace{\left\langle x_{m,n}^{(k)}(t), \mathcal{L}\{x(t-kT_b)\}\right\rangle}_{h_{m,n}^{(k)}} + w_{m,n}^{(k)}, \\ &= b_k h_{m,n}^{(k)} + w_{m,n}^{(k)}. \end{aligned} \tag{14}$$

In (14), $\{h_{m,n}^{(k)}\}$ are the channel coefficients and $\{w_{m,n}^{(k)}\}$ are the noise coefficients. Collecting $\{r_{m,n}^{(k)}\}_{(m,n)\in\mathcal{I}}$ into the vector $\boldsymbol{r}_k$, we can write

$$\boldsymbol{r}_k = b_k \boldsymbol{h}_k + \boldsymbol{w}_k \tag{15}$$

where vectors $\boldsymbol{h}_k$ and $\boldsymbol{w}_k$ are defined similarly. Because the channel produces finite scaling and delay, there is negligible energy in the scale-lag Rake components corresponding to the following set of indices: $\{m,n \mid m > \lceil \frac{\gamma_{\max}}{\gamma_o} \rceil$ or $m < -\lceil \frac{\gamma_{\max}}{\gamma_o} \rceil$, $n > \lceil \frac{\tau_{\sup}}{t_o} \rceil$ or $n < 0\}$. Thus, in the case that $\mathcal{I}$ specifies a rectangular array of Rake fingers with dimension $(2M+1)\times(N+1)$, it would be advisable to choose $M \approx \frac{\gamma_{\max}}{\gamma_o}$ and $N \approx \frac{\tau_{\sup}}{t_o}$ in order to limit complexity while capturing a significant fraction of the received signal energy.

F. Reduced-Complexity Rake Implementation

Anticipating the high expense of accurate wideband analog filtering, we propose a low-complexity means of scale-lag projection. For ease of illustration, we focus on a $(2M+1)\times(N+1)$ rectangular array of Rake fingers. For this setup, we propose to feed the output of a single chip-matched filter into a bank of samplers with rates $\{(a_o^m t_o)^{-1}, m = -M, \ldots, M\}$. Each sampler output is connected to a tapped-delay line with fingers down-sampled to the chip-pulse rate $\frac{1}{T_o}$. (See Fig. 8.) Here, we have assumed, for simplicity, that the chip-spacing T_o is a multiple of the translation-spacing t_o, i.e., $\frac{T_o}{t_o} = N_t$ for $N_t \in \mathbb{N}$. Focusing on the 0^{th} bit and dropping the superscripts in (14), the proposed structure can be justified as follows.

$$\begin{aligned} r_{m,n} &= \int x_{m,n}(t) r(t) dt, \\ &= \frac{1}{a_o^{m/2}} \sum_{i=0}^{N_p-1} \frac{c_i}{\sqrt{N_p}} \int p\left(\tfrac{t - nt_o a_o^m - iT_o a_o^m}{a_o^m}\right) r(t) dt, \\ &= \frac{1}{a_o^{m/2}} \sum_{i=0}^{N_p-1} \frac{c_i}{\sqrt{N_p}} \, p\left(-\tfrac{t}{a_o^m}\right) * r(t)\Big|_{t=(n+iN_t)a_o^m t_o}, \\ &\approx \frac{1}{a_o^{m/2}} \sum_{i=0}^{N_p-1} \frac{c_i}{\sqrt{N_p}} p(-t) * r(t)\Big|_{t=(n+iN_t)a_o^m t_o}, \\ &= \frac{1}{a_o^{m/2}} \sum_{i=0}^{N_p-1} \frac{c_i}{\sqrt{N_p}} z_{m,n}[i], \end{aligned} \tag{16}$$

where $*$ denotes linear convolution and where

$$z_{m,n}[i] := p(-t) * r(t)\Big|_{t=(n+iN_t)a_o^m t_o}. \tag{17}$$

The approximation in (16) is premised on the idea that dilating the T_p-duration chip pulse $p(t)$ by a_o^m has a negligible effect on the Rake outputs.[8] Note that, since $T_b \gg T_p$, dilating $p(t)$ is insignificant in comparison to dilating the T_b-duration bit waveform $x(t)$.

Notice that the translation-spacing t_o is analogous to the sampling period in lag-only Rake reception (i.e., the $m = 0$ components); the scale components (i.e., $m \neq 0$) are obtained by slightly lengthening or shortening the sampling period. An interesting question is how sampling frequency offset will affect the performance of the scale-lag Rake. We conjecture that as long as the sampling of the scale-lag plane is "dense" enough to collect all the received energy, then sampling frequency offsets will not adversely impact performance.

[8] A similar approximation is used for analog-to-digital conversion in a narrowband DSSS system, i.e., the Doppler distortion of chip pulses are ignored [15].

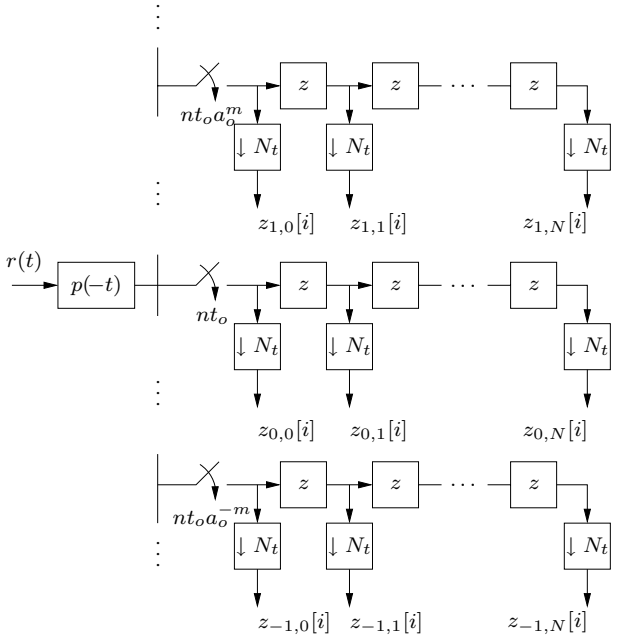

Fig. 8. Block-diagram for the rectangular scale-lag Rake projection given by (16). The receiver can be made causal by introducing an appropriate bulk delay in the matched filter.

IV. Scale-Lag Diversity

To determine the diversity extracted by the coherent scale-lag Rake receiver, we derive the second-order statistics of the wideband channel kernel $\mathcal{L}(a,\tau)$ and use this information to compute correlation between the channel coefficients. The number of *large* eigenvalues of the combining coefficient autocorrelation matrix will be used to study the *effective* diversity order extracted by the receiver.

A. Wideband Scattering Function

In this section, we compute the second-order wideband channel statistics $\mathrm{E}[\mathcal{L}(a,\tau)\mathcal{L}(a',\tau')]$ assuming N discrete independent paths:

$$\mathcal{L}(a,\tau) \;=\; \sum_{n=0}^{N-1} l_n \delta(a-a_n)\delta(\tau-\tau_n), \tag{18}$$

where $\delta(\cdot)$ is the Dirac delta function and where the n^{th} path has real-valued gain l_n, dilation a_n, and lag τ_n. Specifically, we assume:

(A1) The path parameters $\{l_n\}$, $\{a_n\}$, and $\{\tau_n\}$ are i.i.d. across paths with joint density $p_{A,L,\mathcal{T}}(\cdot,\cdot,\cdot)$.
(A2) The path amplitudes are zero mean, i.e., $\mathrm{E}[l_n]=0$.
(A3) The dilation a_n is independent of the amplitude l_n and lag τ_n, i.e., $p_{A,L,\mathcal{T}}(\cdot,\cdot,\cdot)=p_A(\cdot)p_{L,\mathcal{T}}(\cdot,\cdot)$.

Assumption (A3) is motivated by the fact that the amplitude and lag are often correlated in wireless channels, as evident from power profiles that are exponential in the lag variable [12], [34]. Similar assumptions have been made to analyze narrowband channels [35].

From assumptions (A1) and (A2) we write

$$\begin{aligned}&\mathrm{E}[\mathcal{L}(a',\tau')\mathcal{L}(a'',\tau'')]\\ &\quad=\;\mathrm{E}[\delta(a'-a_o)\delta(a''-a_o)N|l_0|^2\delta(\tau'-\tau_0)\delta(\tau''-\tau_0)],\end{aligned} \tag{19}$$

where (A1) allows us to consider the first path without loss of generality. From (A3),

$$\begin{aligned}&\mathrm{E}[\delta(a'-a_o)\delta(a''-a_o)]\\ &\quad=\;\int \delta(a'-a)\delta(a''-a)p_A(a)da,\\ &\quad=\;p_A(a')\delta(a'-a''),\end{aligned} \tag{20}$$

and

$$\begin{aligned}&\mathrm{E}[N|l_0|^2\delta(\tau'-\tau_0)\delta(\tau''-\tau_0)]\\ &\quad=\;N\iint |l|^2\delta(\tau'-\tau)\delta(\tau''-\tau)p_{L,\mathcal{T}}(l,\tau)d\tau dl,\\ &\quad=\;f_{\mathcal{T}}(\tau')\delta(\tau'-\tau''),\end{aligned} \tag{21}$$

where we define

$$f_{\mathcal{T}}(\tau) := Np_{\mathcal{T}}(\tau)\int |l|^2 p_{L|\mathcal{T}}(l|\tau)dl. \tag{22}$$

The function $f_{\mathcal{T}}(\tau)$ is the *delay profile* as a function of lag τ. We substitute (20) and (21) into (19) to obtain

$$\mathrm{E}[\mathcal{L}(a,\tau)\mathcal{L}(a',\tau')] \;=\; \underbrace{p_A(a)f_{\mathcal{T}}(\tau)}_{:=\Psi(a,\tau)}\delta(a-a')\delta(\tau-\tau'), \tag{23}$$

where $\Psi(a,\tau)$ is the *wideband scattering function*, which quantifies the distribution of received power as a function of dilation and delay.

Now that the form of the wideband scattering function has been determined, we investigate the dilation density $p_A(\cdot)$. An often studied channel geometry is a fixed transmitter and dense ring of scatterers surrounding the mobile receiver. In this "isotropic" case, the relation between the angle-of-arrival relative to the direction of travel ξ and dilation a is

$$a \;=\; 1-\gamma_{\max}\cos(\xi). \tag{24}$$

where $\gamma_{\max}=\frac{v_{\max}}{c}$ is the scale-spread. Given the angle of arrival distribution $p_\Xi(\cdot)$, it is a simple matter to compute the dilation distribution $p_A(\cdot)$,

$$p_A(a)=\frac{1}{\gamma_{\max}}p_Y\left(-\frac{a-1}{\gamma_{\max}}\right), \tag{25}$$

where $Y=\cos(\Xi)$ and

$$p_Y(y)=\frac{p_\Xi(\cos^{-1}(y))+p_\Xi(-\cos^{-1}(y))}{\sqrt{1-y^2}}. \tag{26}$$

If the angle of arrival ξ is distributed uniformly on $(-\pi,\pi]$, then we have

$$p_Y(y)=\frac{1}{\pi\sqrt{1-y^2}},\quad |y|<1, \tag{27}$$

which is a shifted version of the familiar "bathtub" profile [36]. We call the function $p_A(a)$ the *scale profile*, analogous to the Doppler profile in narrowband baseband-equivalent channels.

B. Wideband Channel Coefficient Correlation

Recalling (15), the noise vector $\boldsymbol{w}_k$ is Gaussian distributed with zero mean; hence, the optimal bit error rate (BER)-minimizing coherent receiver is the whitened matched filter [12, p. 603], which assumes knowledge of the channel coefficients $\boldsymbol{h}_k$ and noise correlation matrix $\boldsymbol{R_w} := \mathrm{E}[\boldsymbol{w}_k \boldsymbol{w}_k^H] = \sigma_w^2 \boldsymbol{R_x}$, where the elements of $\boldsymbol{R_x}$ are inner products of the form $\langle x_{m,n}^{(k)}(t), x_{m',n'}^{(k)}(t)\rangle$ over $m, m' \in \{-M, \ldots, M\}$ and $n, n' \in \{0, \ldots, N\}$. In practice, the receiver would estimate the channel coefficients $\boldsymbol{h}_k$.

The decision statistic $\hat{b}_k$ is [12]

$$\hat{b}_k = \boldsymbol{f}_k^H (\boldsymbol{R_x}^{-1/2})^H \boldsymbol{r}_k, \tag{28}$$

$$= b_k \|\boldsymbol{f}_k\|^2 + \boldsymbol{f}_k^T (\boldsymbol{R_x}^{-1/2})^H \boldsymbol{w}_k. \tag{29}$$

where $(\boldsymbol{R_x}^{-1/2})^H$ is the whitening matrix and $\boldsymbol{f}_k = (\boldsymbol{R_x}^{-1/2})^H \boldsymbol{h}_k$ is the combining coefficient vector. The matrix $\boldsymbol{R_x}^{1/2}$ is, e.g., the Cholesky decomposition of the matrix $\boldsymbol{R_x}$ and can be computed offline.

In the following, we focus on the k^{th} bit and drop the bit index notation. The signal-to-noise ratio is defined as $\mathsf{SNR} := E_b/\sigma_w^2$ and the theoretical BER expression for a system employing BPSK signaling and coherent reception with perfect channel state information, assuming real-valued Gaussian coefficients, can be computed as [21, pp. 24-25]

$$P_e = \frac{1}{\pi} \int_0^{\pi/2} \prod_{i=0}^{\kappa-1} \left(\frac{\lambda_i \mathsf{SNR}}{\sin^2\theta} + 1 \right)^{-1/2} d\theta, \tag{30}$$

$$\leq \frac{1}{2} \prod_{i=0}^{\kappa-1} (\lambda_i \mathsf{SNR} + 1)^{-1/2}. \tag{31}$$

where $\{\lambda_i\}_{i=1}^{\kappa}$, $\kappa := |\mathcal{I}|$ are the eigenvalues of the combining vector correlation matrix $\boldsymbol{\Sigma} := \mathrm{E}[\boldsymbol{f}\boldsymbol{f}^H] = (\boldsymbol{R_x}^{-1/2})^H \boldsymbol{R}_h \boldsymbol{R_x}^{-1/2}$, and $\boldsymbol{R}_h := \mathrm{E}[\boldsymbol{h}\boldsymbol{h}^T]$ is the the channel autocorrelation matrix.

Similar to [37], we define the *effective diversity order* extracted by the receiver as the negative slope of the log-log plot of P_e versus SNR at a particular finite SNR. An exact expression for the effective diversity order is omitted here because it is complicated and does not yield insight into the connection between the eigenvalues and the BER performance. Instead, the following piecewise-linear upper bound derived from (31) is provided whose negative slope *approximates* the effective diversity order:

$$\log P_e \leq -\frac{B(\mathsf{SNR})}{2} \log \mathsf{SNR} + C(\mathsf{SNR}), \tag{32}$$

where $B(\mathsf{SNR}) := |\{\lambda_j^{\mathsf{big}}\}|$ is the number of large eigenvalues defined as $\{\lambda_j^{\mathsf{big}}\} = \{\lambda_j | \lambda_j > \frac{1}{\mathsf{SNR}}\}$ and $C(\mathsf{SNR}) := \log\frac{1}{2} - \frac{1}{2}\log\prod_{j=0}^{B-1} \lambda_j^{\mathsf{big}}$. We denote the negative slope $\frac{B(\mathsf{SNR})}{2}$ of the upper bound (32) as the *approximate effective diversity order* extracted by the receiver at a particular SNR. Note that $B(\mathsf{SNR})$ is a piecewise-constant function of SNR and that when $\mathsf{SNR} > \frac{1}{\min\{\lambda_i\}_{i=1}^{\kappa}}$, the approximate effective diversity order $\frac{B(\mathsf{SNR})}{2}$ equals the traditionally defined (i.e., asymptotic) diversity order, which, for our real-valued Gaussian channel, is $\frac{\kappa}{2}$, the number of non-zero eigenvalues divided by two.[9]

[9]The halving is an artifact of the real-valued nature of the Gaussian channel coefficients.

To obtain the channel coefficient correlation matrix $\boldsymbol{R}_h$, we use the uncorrelated scattering property (23) to find

$$\mathrm{E}[h_{m,n}^{(k)} h_{m',n'}^{(k')}] = \int_0^{\tau_{\max}} \int_{1-\gamma_{\max}}^{1+\gamma_{\max}} \Psi(a,\tau)\, \mathrm{E}\left[\chi\left(\tfrac{a_o^m}{a}, \tfrac{nt_o a_o^m - \tau - k(a-1)T_b}{a}\right) \chi\left(\tfrac{a_o^{m'}}{a}, \tfrac{n' t_o a_o^{m'} - \tau - k'(a-1)T_b}{a}\right)\right] da d\tau,$$

$$\approx \int_0^{\tau_{\max}} \int_{1-\gamma_{\max}}^{1+\gamma_{\max}} \Psi(a,\tau) \bar{\chi}\left(\tfrac{a_o^m}{a}, \tfrac{nt_o a_o^m - \tau - k(a-1)T_b}{a}\right) \bar{\chi}\left(\tfrac{a_o^{m'}}{a}, \tfrac{n' t_o a_o^{m'} - \tau - k'(a-1)T_b}{a}\right) da d\tau, \tag{33}$$

The approximation above is due to Lemma 4 in Appendix I, which makes the case that $\mathrm{E}[\chi(a,\tau)\chi(a',\tau')] \approx \bar{\chi}(a,\tau)\bar{\chi}(a',\tau')$ when a and a' are near unity and N_p is large. With the approximations[10] $\frac{a_o^m}{a} \approx 1 + m\gamma_o - (a-1)$ and $\frac{nt_o a_o^m - \tau - i(a-1)T_b}{a} \approx nt_o - \tau - i(a-1)T_b$, the correlation (33) can be approximated by

$$\mathrm{E}[h_{m,n}^{(k)} h_{m',n'}^{(k')}] \approx \int_0^{\tau_{\max}} \int_{1-\gamma_{\max}}^{1+\gamma_{\max}} \Psi(a,\tau)\, \bar{\chi}\left(1 + m\gamma_o - (a-1), nt_o - \tau - k(a-1)T_b\right) \bar{\chi}\left(1 + m'\gamma_o - (a-1), n' t_o - \tau - k'(a-1)T_b\right) da d\tau.$$

We insert the parameterizations $t_o = \frac{k_\tau}{f_o}$ and $\gamma_o = \frac{k_\gamma}{T_b f_o}$ from Section III-B and make the substitutions $\bar{\gamma} := \frac{a-1}{(T_b f_o)^{-1}}$ and $\bar{\tau} := \frac{\tau}{f_o^{-1}}$, for *normalized scale* and *normalized lag*, respectively, to obtain

$$\mathrm{E}[h_{m,n}^{(k)} h_{m',n'}^{(k')}] \approx \frac{1}{T_b f_o^2} \int_0^{\tau_{\max} f_o} \int_{-\gamma_{\max} T_b f_o}^{\gamma_{\max} T_b f_o} \Psi\left(1 + \frac{\bar{\gamma}}{T_b f_o}, \frac{\bar{\tau}}{f_o}\right) \int_0^1 \chi_p\left(1, \tfrac{nk_t - \bar{\tau} + (mk_\gamma - \bar{\gamma})z - k\bar{\gamma}}{f_o}\right) dz \int_0^1 \chi_p\left(1, \tfrac{n' k_t - \bar{\tau} + (m' k_\gamma - \bar{\gamma})z' - k'\bar{\gamma}}{f_o}\right) dz' d\bar{\gamma} d\bar{\tau}, \tag{34}$$

where we used $\bar{\chi}(a,\tau)$ from (10). The channel correlation matrix $\boldsymbol{R_h}$ can be constructed component-wise from (34) with $k = k' = 0$.

V. Numerical Results

In this section, we examine the BER performance of a DSSS system employing a unit-energy second-derivative Gaussian chip pulse (c.f. (8)). We assume an energy-preserving channel, i.e., $\iint \Psi(a,\tau) da d\tau = 1$, with real-valued Gaussian coefficients that satisfy (A1)-(A3), so that the results in Section IV apply. By central limit theory arguments, the Gaussian coefficient property can be justified through the assumption that each channel coefficient represents an aggregate of many reflections. BER is calculated using (30) and plotted against $\mathsf{SNR} = \frac{E_b}{\sigma_w^2}$. To obtain the eigenvalues in (30), we computed $\boldsymbol{R_h}$ in (34) by numerically integrating over the variables $(\bar{\gamma}, \bar{\tau})$ using a 41×41 grid and MATLAB's `trapz` command.

[10]Note that $a_o^m \approx 1 + m\gamma_o$ and $1/a \approx 1 - (a-1)$ for $a \approx 1$.

Figure 9 compares performances of the rectangular and "T-shaped" scale-lag Rakes to a rectangular frequency-lag Rake and a lag-only Rake. Our baseband channel mandates that we use a real-valued version of the frequency-lag Rake from [15], the details of which are given in Appendix II. The lag-only Rake employs a linear array of $N+1$ fingers, the "T-shaped" Rake employs $N+1$ lag fingers plus two non-trivial scale fingers, as illustrated in Fig. 7, and the rectangular Rakes employ an array of $(2M+1)\times(N+1)$ fingers.

For the scale and lag spacing of the scale-lag Rake fingers, we chose $k_\gamma = 0.28$ (equivalent to half the minimum resolvable dilation) and $k_\tau = 0.236$ (equivalent to the minimum resolvable lag), respectively. Smaller scale and lag spacings were found to yield little performance gain due to increasing correlations between Rake fingers; larger scale and lag spacings led to a degradation in performance. We chose $M = \lceil \frac{\gamma_{\max}}{\gamma_o} \rceil = \lceil \frac{\gamma_{\max} T_b f_o}{k_\gamma} \rceil$ and $N = \lceil \frac{\tau_{\sup}}{t_o} \rceil = \lceil \frac{\tau_{\sup} f_o}{k_\tau} \rceil$ to ensure that the majority of the signal energy was captured by the receiver. The experiments were performed with a "bathtub-shaped" scale profile[11] (27) and a (truncated) exponential delay profile $f_{\mathcal{T}}(\tau) = Ke^{-\alpha\tau}$ for $0 \le \tau \le \tau_{\sup}$ and $f_{\mathcal{T}}(\tau) = 0$ otherwise, where $\alpha = \frac{\ln(4)}{\tau_{\sup}}$ and $K = \frac{\alpha}{1-\exp(-\alpha\tau_{\sup})}$. The normalized effective delay spread was $\tau_{\sup} f_o = 0.5$ and normalized scale spread was chosen from $\gamma_{\max} T_b f_o \in \{0.005, 0.05, 0.1\}$. Recalling the examples given in Section II, $\gamma_{\max} T_b f_o = 0.01$ and $\tau_{\sup} f_o = 0.5$ would occur in a 2-ray RF system with mobile velocity 67.5 km/hr, data rate 25 kbps, and bandwidth 8 GHz; or in an underwater system with mobile velocity 11 km/hr, data rate 10 bps, bandwidth 100 Hz, and delay spread of 10 ms. In both of these examples, $\tau_{\max} \ll T_b$, so that ISI can be prevented using guardbands that are much shorter than the bit interval.

In Fig. 9(a), the normalized scale spreading $\gamma_{\max} T_b f_o = 0.005$ is minimal, and so the four receivers show similar performance. In Figures 9(b) and (c), with normalized scale-spreads of $\gamma_{\max} T_b f_o = 0.05$ and 0.1, respectively, the scale-lag Rake exploits an approximate effective diversity order of three at SNR$=30$ dB, while the lag-only Rake exploits only an approximate effective diversity order of two at the same SNR. The approximate effective diversity orders can be determined by counting the number of eigenvalues above -30 dB and dividing by two [c.f. (32)]. The frequency-lag Rake also exploits an approximate effective diversity order of three, though with smaller eigenvalues and hence worse BER performance. Note that the "T-shaped" scale-lag Rake performs nearly as well as the frequency-lag Rake, and much better than the lag-only Rake with only a slight increase in complexity.

For the remainder of this section, we report Monte Carlo results that verify the above theoretical results. The setup and results are described in the following paragraphs.

The DSSS signal was specified by the following parameters: $T_p = T_o = \frac{2}{f_o}$, where f_o is the frequency of the chip-pulse's spectral peak, T_p is the chip-pulse duration, and T_o is the chip-pulse spacing. While, in practical systems, the chip-pulses might be spaced farther apart, complexity precluded us from doing so. The second-derivative Gaussian pulse (8) was chosen as the chip pulse, and the spreading sequence $\{c_i\}_{i=0}^{N_p-1}$ was a random binary sequence of length $N_p = 128$.

[11]Here we assume a uniform angle-of-arrival distribution; practical systems may deviate from this assumption.

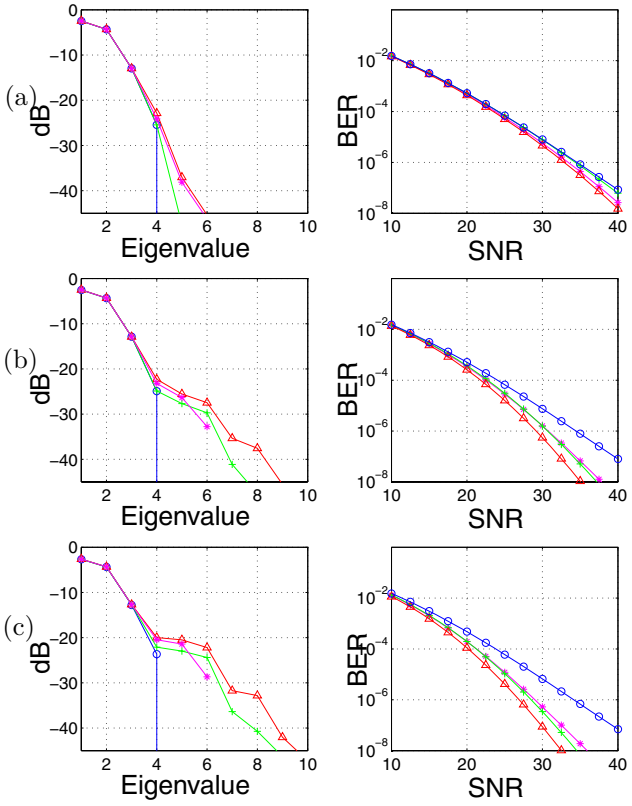

Fig. 9. For the scale-spacing relation $k_\gamma = 0.28$ (set to half the minimum scale resolution) and translation-spacing relation $k_\tau = 0.236$ (set to minimum resolvable lag), we compare the eigenvalues and BER performances of the receivers for the "bathtub"-shaped scale profile (27) with scale-spreads of (a) $\gamma_{\max} T_b f_o = 0.005$, (b) $\gamma_{\max} T_b f_o = 0.05$, (c) $\gamma_{\max} T_b f_o = 0.1$, and an exponential delay profile truncated to an effective delay spread of $\tau_{\sup} f_o = 0.5$. The curves are described as follows: ($\circ$) the lag-only Rake, (+) the "T-shaped" scale-lag Rake shown in Fig. 7(b), ($*$) the real-valued rectangular frequency-lag Rake from Appendix II, and ($\triangle$) the scale-lag Rake.

An $N = 10$ tap random dilation-delay channel was generated with a "bathtub"-shaped scale profile $p_A(a)$ and with a truncated exponential lag profile $f_{\mathcal{T}}(\tau)$. The dilations and delays for each tap were chosen uniformly over the non-zero support of the respective profiles, and the tap amplitudes were zero-mean Gaussian distributed with variance satisfying the scale-lag power profile. The normalized scale spread was $\gamma_{\max} T_b f_o = 0.1$, and the normalized effective delay spread was $\tau_{\sup} f_o = 0.5$. In total, 25000 channel realizations were generated and each realization consumed approximately 500000 multiplies.[12]

The channel coefficients $\boldsymbol{h}^T := [h_{-M,0}, \ldots, h_{M,N}]$ were obtained by projecting the noiseless received signal onto the

[12]We would like to point out that a high simulation complexity does not necessarily imply a high receiver complexity. Our wideband DSSS simulations are numerically intensive because the *sampling rate* required to simulate wideband signaling is inherently high; there is no simplifying "baseband equivalent representation" as there would be with a carrier-modulated narrowband system.

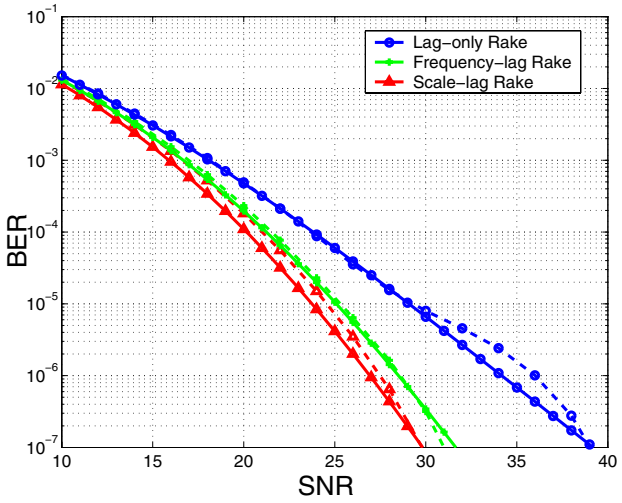

Fig. 10. Theoretical and simulated BER performances of the receivers with scale- and translation-spacing relations as in Fig. 9. The normalized scale spread is $\gamma_{\max} T_b f_o = 0.1$, and the normalized effective delay spread is $\tau_{\sup} f_o = 0.5$. The solid curves indicate theoretical performance (c.f. equation (30)) and the dashed curves indicate simulated performance (see the description of the simulation above).

Rake basis functions. The projections were calculated using the discrete approximation

$$\begin{aligned} h_{m,n} &= \int x_{m,n}(t) r(t) dt \\ &\approx \sum_{i=0}^{N_{\text{samps}}-1} x_{m,n}(iT_s) r(iT_s) T_s, \end{aligned} \tag{35}$$

where T_s was the sampling period. For the simulations, we chose $T_s = \frac{1}{15 f_o}$, which implies approximately 30 samples per chip-pulse.

The Monte-Carlo bit error probability was computed via

$$P_e(\mathsf{SNR}) := \mathrm{E}\left[Q\left(\sqrt{\|\boldsymbol{f}\|^2 \mathsf{SNR}}\right)\right] \tag{36}$$

$$\approx \frac{1}{N_{\text{sim}}} \sum_{a=1}^{N_{\text{sim}}} Q\left(\sqrt{\|\boldsymbol{f}_a\|^2 \mathsf{SNR}}\right) \tag{37}$$

where $\mathsf{SNR} := \frac{E_b}{\sigma_w^2}$, $\boldsymbol{f}_a := (\boldsymbol{R}_{\boldsymbol{x}}^{-1/2})^H \boldsymbol{h}_a$ denotes a^{th} realization of the combining coefficients vector, and N_{sim} denotes the number of channel realizations. The Monte Carlo curves in Fig. 10 match the theoretical with reasonable accuracy.

VI. Conclusions

In this paper, we studied *scale-lag* Rake receivers capable of leveraging the diversity that results from scale-lag spreading in mobile wideband direct-sequence spread-spectrum (DSSS) systems. Our analysis applies to mobile channels where narrowband fractional-bandwidth assumptions are invalid, such as radio-frequency ultra-wideband (UWB) systems and underwater wideband acoustic systems. After defining the *minimum scale resolution* of a DSSS signal, we produced guidelines for choosing the scale-spacing and lag-spacing parameters for the scale-lag Rake basis. We derived the wideband scattering function for a uniform ring of scatterers and used this to numerically compute the performances of scale-lag, frequency-lag, and conventional lag-only Rakes. The proposed scale-lag Rake receiver outperformed the frequency-lag Rake with an equal number of fingers, since the scale-lag Rake was better matched to the scale-lag spreading of the wideband channel. Both scale-lag and frequency-lag Rakes outperformed the lag-only Rake in the presence of mobility.

Appendix I
Proof of Proposition 1 and 2

In this appendix, we establish three lemmas and then use them to prove Propositions 1 and 2.

Lemma 3: $\mathrm{E}[\chi(a,\tau)] \approx \bar{\chi}(a,\tau)$ for large N_p and $a \approx 1$.

Proof: Assuming unit-variance zero-mean uncorrelated $\{c_i\}$, we write

$$\begin{aligned} &\mathrm{E}\left[\chi(a,\tau)\right] \\ &= \mathrm{E}\left[\int_{-\infty}^{\infty} x(t) \frac{1}{\sqrt{a}} x\left(\frac{t-\tau}{a}\right) dt\right], \\ &= \sum_{i=0}^{N_p-1} \frac{\mathrm{E}[c_i^2]}{N_p \sqrt{a}} \int_{-\infty}^{\infty} p(t) p\left(\frac{t-\tau-(a-1)iT_o}{a}\right) dt. \\ &= \sum_{i=0}^{N_p-1} \frac{1}{N_p} \chi_p\left(a, \tau + (a-1)iT_o\right) \end{aligned} \tag{38}$$

where the chip pulse ambiguity function $\chi_p(a,\tau)$ is defined in (11). Using $T_o = \frac{T_b}{N_p}$, the summation in (38) is well approximated by an integral when N_p is large:

$$\begin{aligned} &\sum_{i=0}^{N_p-1} \frac{1}{N_p} \chi_p\left(a, \tau + (a-1)\frac{i}{N_p} T_b\right) \\ &\quad \approx \int_0^1 \chi_p(a, \tau + (a-1) z T_b) dz. \end{aligned} \tag{39}$$

When $a \approx 1$, (39) can be further approximated as

$$\begin{aligned} &\int_0^1 \chi_p(a, \tau + (a-1) z T_b) dz \\ &\quad \approx \int_0^1 \chi_p(1, \tau + (a-1) z T_b) dz, \\ &\quad = \bar{\chi}(a,\tau). \end{aligned} \tag{40}$$

■

Lemma 4: $\mathrm{E}[\chi(a,\tau)\chi(a',\tau')] \approx \bar{\chi}(a,\tau)\bar{\chi}(a',\tau')$ for large N_p and $a \approx 1$.

Proof: We start with

$$\begin{aligned} &\mathrm{E}[\chi(a,\tau)\chi(a',\tau')] \\ &\quad = \frac{1}{N_p^2} \sum_{i,j,k,l} \mathrm{E}[c_i c_j c_k c_l] \\ &\qquad \chi_p(a, \tau + (ai-j)T_o) \chi_p(a', \tau' + (a'k-l)T_o), \end{aligned} \tag{41}$$

with $\chi_p(a,\tau)$ defined in (11). The expectation in (41) reduces to

$$\mathrm{E}[c_i c_j c_k c_l] = \begin{cases} \mathrm{E}[c_i^4] & i=j=k=l, \\ \mathrm{E}[c_i^2]^2 & i=j,\ k=l,\ i \neq k, \\ \mathrm{E}[c_i^2]^2 & i=k,\ j=l,\ i \neq j, \\ \mathrm{E}[c_i^2]^2 & i=l,\ j=k,\ i \neq j, \\ 0 & \text{else.} \end{cases} \tag{42}$$

Using $T_o = \frac{T_b}{N_p}$, we shall see that only the second case in (42) yields a non-negligible contribution.

The terms in (41) corresponding to $\{i = j = k = l\}$ can be upper bounded by

$$\sum_{i=0}^{N_p-1} \frac{\mathrm{E}[c_i^4]}{N_p^2} \left| \chi_p\left(a, \tau+(a-1)\frac{i}{N_p}T_b\right) \chi_p\left(a', \tau'+(a'-1)\frac{i}{N_p}T_b\right)\right| \leq \frac{\mathrm{E}[c_i^4]}{N_p}, \quad (43)$$

where the inequality in (43) follows from the chip pulse having bounded energy, i.e., $|\chi_p(a,\tau)| \leq 1$. Note that, for large N_p, (43) becomes negligible. Next, the summation terms in (41) corresponding to $\{i = j,\ k = l,\ i \neq k\}$ can be approximated, for large N_p as

$$\begin{aligned} &\sum_{i,k\neq i} \frac{\mathrm{E}[c_i^2]^2}{N_p^2} \chi_p\left(a, \tau+(a-1)\frac{i}{N_p}T_b\right) \chi_p\left(a, \tau'+(a'-1)\frac{k}{N_p}T_b\right) \\ &\approx \mathrm{E}[c_i^2]\int_0^1 \chi_p(1, \tau+(a-1)zT_b)dz \; \mathrm{E}[c_i^2]\int_0^1 \chi_p(1, \tau'+(a'-1)z'T_b)dz' \\ &= \bar{\chi}(a,\tau)\bar{\chi}(a',\tau'), \end{aligned} \quad (44)$$

while those corresponding to $\{i = k,\ j = l,\ i \neq j\}$ can be approximated, for $a \approx 1$, by

$$\begin{aligned} &\sum_{i,j\neq i} \frac{\mathrm{E}[c_i^2]^2}{N_p^2} \left| \chi_p\left(a, \tau+(ai-j)T_o\right) \chi_p\left(a', \tau'+(a'i-j)T_o\right)\right| \\ &\approx \sum_{i,j} \frac{\mathrm{E}[c_i^2]^2}{N_p^2} \left| \chi_p\left(1, \tau+(ai-j)T_o\right) \chi_p\left(1, \tau'+(a'i-j)T_o\right)\right| \quad (45) \\ &\leq \sum_{i=0}^{N_p-1} \frac{2\,\mathrm{E}[c_i^2]^2}{N_p^2} = \frac{2\,\mathrm{E}[c_i^2]^2}{N_p}. \quad (46) \end{aligned}$$

The following arguments justify (46). Since $p(t)$ is time-limited to T_p seconds, $\chi_p(1,z)$ is non-zero only when $|z| < T_p$. Therefore, fixing a and τ, for each $i \in \{1, 2, \ldots, N_p - 1\}$, there are at most two values of j such that $|\frac{\tau}{T_o}+ai-j| < \frac{T_p}{T_o}$. This property, combined with $|\chi_p(a,\tau)| < 1$, leads to the inequality in (46). Note that, for large N_p, the component in (46) becomes negligible. Finally, the summation terms in (41) corresponding to $\{i = l,\ j = k,\ i \neq j\}$ can also be shown to negligible using similar arguments. In summary, only (44) yields a non-negligible contribution to (41), so that $\mathrm{E}[\chi(a,\tau)\chi(a',\tau')] \approx \bar{\chi}(a,\tau)\bar{\chi}(a',\tau')$. ■

Lemma 5: For N_p large and a near unity, the wideband ambiguity function $\chi(a,\tau)$ is approximately equal to $\bar{\chi}(a,\tau)$ in the mean-squared sense.

Proof: Lemmas 3 and 4 imply

$$\begin{aligned} &\mathrm{E}[|\chi(a,\tau) - \bar{\chi}(a,\tau)|^2] \\ &= \mathrm{E}[(\chi(a,\tau))^2] - 2\,\mathrm{E}[\chi(a,\tau)]\bar{\chi}(a,\tau) + (\bar{\chi}(a,\tau))^2 \\ &\approx 0. \end{aligned} \quad (47)$$

■

A. Proposition 1

Proof: From Lemma 5, we see that $\bar{\chi}(1,\tau)$ is a mean-square approximation of $\chi(1,\tau)$; hence, from (10)

$$\begin{aligned} \chi(1,\tau) &\approx \int_0^1 \chi_p(1,\tau)dz \quad (48) \\ &= \chi_p(1,\tau). \quad (49) \end{aligned}$$

The function $\chi_p(1,\tau) = 0$ when $\tau > T_p$. ■

B. Proposition 2

Proof: From Lemma 5, we see that $\bar{\chi}(a,0)$ is a mean-square approximation of $\chi(a,0)$; hence, from (10)

$$\begin{aligned} \chi(a,0) &\approx \int_0^1 \chi_p(1,(a-1)zT_b)dz \quad (50) \\ &= \int_0^1 R_p((a-1)zT_b)dz \quad (51) \\ &= \frac{1}{2(a-1)T_b}\int_{-(a-1)T_b}^{(a-1)T_b} R_p(z)dz. \quad (52) \end{aligned}$$

where $R_p(\tau) := \chi_p(1,\tau)$ is the deterministic autocorrelation function of the chip pulse $p(t)$. Suppose $S_p(0) = 0$ where $S_p(f)$ is the energy spectral density of the chip pulse. Since the chip pulse has time support of T_p seconds, then for $(a-1)T_b \geq T_p \Leftrightarrow a \geq 1 + \frac{T_p}{T_b}$ we have

$$\chi(a,\tau) \approx S_p(0) = 0,$$

for N_p large and a near unity. ■

APPENDIX II
REAL-VALUED FREQUENCY-LAG BASIS

The real-valued frequency-lag basis is a simple modification of the work in [15], which is included here to facilitate comparison to our baseband scale-lag Rake. The frequency-lag basis functions are uniform frequency- and time-shifted versions of the DSSS waveform:

$$\tilde{x}_{m,n}(t) := \tilde{y}_m(t/T_b)x(t-nt_o) \quad (53)$$

where

$$\tilde{y}_m(t) := \begin{cases} \sqrt{2}\cos(2\pi mt) & m > 0, \\ -\sqrt{2}\sin(2\pi mt) & m < 0, \\ 1 & m = 0. \end{cases} \quad (54)$$

In [15], it is shown that the baud-spaced complex-valued extension of the frequency-lag basis (53) is approximately orthonormal, which motivated using the frequency-lag Rake receiver to extract diversity in doubly-spread narrowband baseband-equivalent channels.

REFERENCES

[1] J. Taylor, "Ultrawideband radar," *IEEE MTT-S International Microwave Symposium Digest*, vol. 1, pp. 367–370, June 1991.

[2] Federal Communications Commission, "Revision of part 15 of the commission's rules regarding ultra-wideband transmission systems, First report and order," ET Docket 98-153, FCC 02-48, pp. 1–118, Feb. 14, 2002.

[3] R. Balan, H. V. Poor, S. Rickard, and S. Verdú, "Time-frequency and time-scale canonical representations of doubly spread channels," *Proc. European Signal Processing Conf.*, Sep. 2004, pp. 445–448.

[4] J. Davies, S. Pointer, and S. Dunn, "Wideband acoustic communications dispelling narrowband myths," in *OCEANS 2000 MTS/IEEE Conf. Exhibition*, Sep. 2000, vol. 1, pp. 377–384.

[5] M. Win and R. Scholtz, "Ultra-wide bandwidth time-hopping spread-spectrum impulse radio for wireless multiple-access communications," *IEEE Trans. Commun.*, vol. 48, pp. 679–689, Apr. 2000.

[6] G. Hariharan and A. M. Sayeed, "Minimum probability of error in sparse wideband channels," in *Proc. Allerton Conf. Commun., Control, Computing*, Sep. 2006.

[7] B. M. Sadler and A. Swami, "On the performance of episodic UWB and direct-sequence communication systems," *IEEE Trans. Wireless Commun.*, vol. 3, pp. 2246–2255, Nov. 2004.

[8] M. Antweiler, L. Bomer, and H.-D. Luke, "Perfect ternary arrays," *IEEE Trans. Inform. Theory*, vol. 36, pp. 696–705, May 1990.

[9] D. Wu, P. Spasojevic, and I. Seskar, "Ternary zero correlation zone sequences for multiple code UWB," in *Proc. Conf. Inform. Science Syst.*, Mar. 2004, pp. 939–943.

[10] S. Rickard, "Time-frequency and time-scale representations of doubly spread channels," PhD thesis, Princeton University, Nov. 2003.

[11] J. F. Kepler, T. P. Krauss, and S. Mukthavaram, "Delay spread measurements on a wideband MIMO channel at 3.7 GHz," in *Proc. IEEE Veh. Technol. Conf.*, Sep. 2002, pp. 2498–2502.

[12] J. Proakis, *Digital Communications*, 4th ed. New York: McGraw-Hill, 2001.

[13] M. Stojanovic, "Recent advances in high-speed underwater acoustic communications," *IEEE J. Oceanic Engineering*, vol. 21, pp. 125–136, Apr. 1996.

[14] L. Yang and G. B. Giannakis, "Ultra-wideband communications: An idea whose time has come," *IEEE Signal Processing Mag.*, pp. 26–55, Nov. 2004.

[15] A. M. Sayeed and B. Aazhang, "Joint multipath-Doppler diversity in mobile wireless communications," *IEEE Trans. Commun.*, vol. 47, pp. 123–132, Jan. 1999.

[16] Y. Jiang and A. Papandreou-Suppappola, "Time-scale cononical model for wideband system characterization," in *Proc. IEEE Int. Conf. Acoustics, Speech, Signal Processing*, Mar. 2005, pp. 281–284.

[17] Q. Jin, K. M. Wong, and Z.-Q. Luo, "The estimation of time delay and Doppler stretch of wideband signals," *IEEE Trans. Signal Processing*, vol. 43, pp. 904–916, Apr. 1995.

[18] A. Swami, B. Sadler, and J. Turner, "On the coexistence of ultra-wideband and narrowband radio systems," in *Proc. IEEE Military Commun. Conf.*, Oct. 2001, vol. 1, pp. 16–19.

[19] J. Conroy, J. LoCicero, and D. Ucci, "Communication techniques using monopulse waveforms," in *Proc. IEEE Military Commun. Conf.*, Oct 1999, vol. 2, pp. 1181–1185.

[20] L. Zhao and A. Haimovich, "Performance of ultra-wideband communications in the presence of interference," *IEEE J. Select. Areas Commun.*, vol. 20, pp. 1684–1691, Dec. 2002.

[21] A. R. Margetts, "Joint scale-lag diversity in mobile wideband communications," PhD thesis, The Ohio State University, 2005.

[22] S. Mallat, *A Wavelet Tour of Signal Processing*, 2nd ed. San Diego: Academic Press, 1999.

[23] M. K. Tsatsanis and G. B. Giannakis, "Time-varying system identification and model validation using wavelets," *IEEE Trans. Signal Processing*, vol. 41, pp. 3512–3523, Dec. 1993.

[24] M. Martone, "Wavelet-based separating kernels for sequence estimation with unknown rapidly time-varying channels," *IEEE Commun. Lett.*, vol. 3, pp. 78–80, Mar. 1999.

[25] L. G. Weiss, "Wavelets and wideband correlation processing," *IEEE Signal Processing Mag.*, pp. 13–32, Jan. 1994.

[26] F.-Y. Lin and J.-M. Liu, "Ambiguity functions of laser-based chaotic radar," *IEEE J. Quantum Electronics*, vol. 40, pp. 1732–1738, Dec. 2004.

[27] A. Fuxjaeger and R. Iltis, "Acquisition of timing and Doppler-shift in a direct-sequence spread-spectrum system," *IEEE Trans. Commun.*, vol. 42, pp. 2870–2880, Oct. 1994.

[28] G. Kaiser, "Physical wavelets and radar: A variational approach to remote sensing," *IEEE Antennas Propagat. Mag.*, vol. 38, pp. 15–24, Feb. 1996.

[29] M. Dawood and R. Narayanan, "Generalised wideband ambiguity function of a coherent ultrawideband random noise radar," *IEE Radar, Sonar Navigation*, vol. 150, pp. 379–386, Oct. 2003.

[30] R. Scholtz and J.-Y. Lee, "Problems in modeling UWB channels," in *Proc. Asilomar Conf. Signals, Syst., Computers*, vol. 1, pp. 706–711, Nov. 2002.

[31] J.-Y. Lee and R. A. Scholtz, "Ranging in dense multipath environment using an UWB radio link," *IEEE J. Select. Areas Commun.*, vol. 20, pp. 1677–1683, Dec. 2002.

[32] J. Ovarlez, "Cramer-Rao bound computation for velocity estimation in the broad band case using the mellin transform," in *Proc. IEEE Int. Conf. Acoust., Speech, Signal Processing*, Apr. 1993, pp. 273–276.

[33] J. Bartrand, P. Bertrand, and J.-P. Ovarlez, *The Transforms and Applications Handbook*, 2nd ed., ch. 11, pp. 1–11. CRC Press LLC, 2000.

[34] M. Terri, A. Hong, G. Guibe, and F. Legrand, "Major characteristics of UWB indoor transmission for simulation," in *Proc. IEEE Veh. Technol. Conf.*, vol. 1, pp. 19–23, Apr. 2003.

[35] G. L. Stuber, *Principles of Mobile Communications*. Norwell, MA: Kluwer Academic, 1996.

[36] W. Jakes, *Microwave Mobile Communications*. Piscataway, NJ: IEEE Press, 1993.

[37] R. Narasimhan, "Finite-SNR diversity-multiplexing tradeoff for correlated Rayleigh and Rician MIMO channels," *IEEE Trans. Inform. Theory*, vol. 52, pp. 3965–3979, Sep. 2006.

Adam R. Margetts received a dual B.S. degree in Electrical Engineering and Mathematics from Utah State University, Logan, UT in 2000; and the M.S. and Ph.D. degrees in Electrical Engineering from The Ohio State University, Columbus, OH in 2002 and 2005, respectively. Dr. Margetts is currently with MIT Lincoln Laboratory, Lexington, MA, and his research interests include adaptive filtering, ultra-wideband and MIMO communications, and wireless networking.

Philip Schniter received the B.S. and M.S. degrees in Electrical and Computer Engineering from the University of Illinois at Urbana-Champaign in 1992 and 1993, respectively. From 1993 to 1996 he was employed by Tektronix Inc. in Beaverton, OR as a systems engineer. In 2000, he received the Ph.D. degree in Electrical Engineering from Cornell University in Ithaca, NY. Subsequently, he joined the Department of Electrical and Computer Engineering at The Ohio State University in Columbus, OH, where he is now an Associate Professor. In 2003, he received the National Science Foundation CAREER Award, and he currently serves on the IEEE Signal Processing for Communications Technical Committee. Dr. Schniter's research interests include signal processing, communication theory, and wireless networks.

Ananthram Swami received the B.Tech. degree from IIT, Bombay; the M.S. degree from Rice University, Houston; and the Ph.D. degree from the University of Southern California (USC), all in Electrical Engineering. He has held positions with Unocal Corporation, USC, CS-3 and Malgudi Systems. He was a Statistical Consultant to the California Lottery, developed a Matlab-based toolbox for non-Gaussian signal processing, and has held visiting faculty positions at INP, Toulouse. He is currently with the US Army Research Laboratory where his work is in the broad area of signal processing, wireless communications and networking, including both sensor networks and MANETs.